



Optics Letters

Strain-based tunable optical microresonator with an in-fiber rectangular air bubble

SHEN LIU,^{1,2} ZHONGYUAN SUN,^{1,2} LIN ZHANG,² CAILING FU,¹ YU LIU,^{3,4} CHANGRUI LIAO,¹ JUN HE,¹ ZHIYONG BAI,¹ YING WANG,¹ AND YIPING WANG^{1,*}

¹Key Laboratory of Optoelectronic Devices and Systems of Ministry of Education and Guangdong Province, College of Optoelectronic Engineering, Shenzhen University, Shenzhen 518060, China

²Aston Institute of Photonic Technologies, Aston University, Birmingham, UK

³College of Optoelectronic Engineering, Chongqing University of Posts and Telecommunications, Chongqing, China

⁴e-mail: liuyu@cqupt.edu.cn

*Corresponding author: ypwang@szu.edu.cn

Received 29 May 2018; revised 25 July 2018; accepted 25 July 2018; posted 26 July 2018 (Doc. ID 332976); published 16 August 2018

We demonstrate a strain-based fully tunable, near-lossless, whispering gallery mode (WGM) resonator made of an in-fiber rectangular air bubble, which is fabricated by splicing two segments of standard single-mode fibers. Such a resonator, with a 39 μm order radius and 1 μm order wall thickness, contributes to a high quality factor exceeding 10^6 . The tuning in resonant wavelength is achieved by applying tensile strain to the resonator, and the voltage-tuning rate of the WGM resonance peaks is about 31.96 pm/V (strain-tuning rate ~ 14.12 pm/ $\mu\epsilon$), and the corresponding tuning accuracy is better than 0.03 pm. Since the tensile strain applied on the resonator can reach 1000 $\mu\epsilon$, the achievable total tunable bandwidth of ~ 14.12 nm is more than two times that of its azimuthal free spectral range. © 2018 Optical Society of America

OCIS codes: (230.5750) Resonators; (060.2370) Fiber optics sensors; (220.4000) Microstructure fabrication; (060.4005) Microstructured fibers.

<https://doi.org/10.1364/OL.43.004077>

Optical whispering gallery mode (WGM) resonators, with a combination of high quality factor (Q) and small mode volume of modes, have great potential for growth in many research and technology fields [1] such as microlasers [2–4], biosensors [5,6], chemical sensing [7], and interfaces for quantum communication [8,9]. A variety of resonators are currently demonstrated, covering the structures of microspheres [10], microtoroids [6], microrings [11], and mirobubbles [12]. These resonators typically confine the light in a narrow ring along its equator surface by continuous total internal reflection. While such equatorial WGMs have the advantage of a small mode volume, they also exhibit large wavelength spacing between consecutive modes [13]. Furthermore, for many of these applications, matching a resonant mode to a narrow wavelength range is required. One of the direct methods to preselect the WGM resonant wavelength is by means of the size design of

the resonator. However, the fabrication limitations hinder precise control over a mode peak position. Another method is to directly tune the already generated resonant mode. Therefore, various methods to tune the resonator have been reported currently, examples including applying strain [13–17], pressure [15,18], electric fields [19,20], magnetic fields [21], and bending [22].

In this Letter, for the first time, to the best of our knowledge, we propose and experimentally demonstrate a novel high- Q microresonator based on an in-fiber rectangular air bubble (RAB) structure, and its WGM resonance tunability by applying tensile strain. Such a microresonator, with a diameter of 78 μm along its equator surface and an ultrathin wall thickness of 1 μm , is created by splicing two sections of standard single-mode fibers [23]. We have successfully demonstrated the possibility of a reliable continuous tuning of WGMs in the resonator by simply applying the tensile strain to the structure, and a tunability of 31.96 pm/V is achieved, giving a tunable bandwidth of 14.12 nm. The microresonator has also exhibited a superbroad tunable range, which is over two times larger than that of its azimuthal free spectral range (FSR). In our experiment, the achieved quality factor of the resonator exceeds 10^6 , and the WGM is recognized as near-lossless.

As shown in Fig. 1(a), an RAB, as a resonator, has a diameter ($2R_0$) of 78 μm along its equator surface and a maximum cavity length of 85 μm along the fiber axis that have been measured from an optical microscope image. This RAB is fabricated by means of splicing together two sections of standard single-mode fiber and tapering the splicing joint, and the detailed fabrication process is described in Refs. [23,24]. It is noteworthy that in the whole fabrication process of the RAB, only a common fusion splicer was employed, and no additional device was required as in using a CO_2 laser beam, pressurization, or convective heating in a flame and furnace [12,14]. To determine the fabrication limit of the silica diaphragm thickness, the RAB was cut open at the A-point labeled on the equator surface [Fig. 1(a)] by using femtosecond laser micromachining. A scanning electron microscope (SEM) image, shown in the inset of Fig. 1(a),

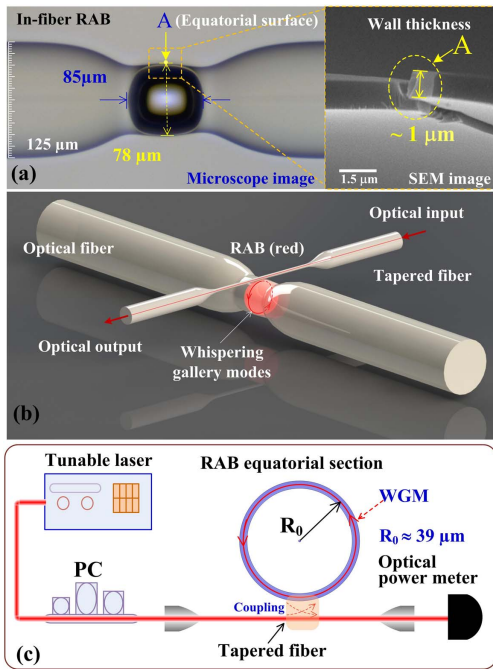


Fig. 1. (a) Optical microscope image of an in-fiber RAB; inset, the cut-plane SEM image of the RAB. (b) Schematic diagram of a taper fiber-coupled microresonator. (c) Schematic of the experimental setup; PC, polarization controller.

gives a measured wall thickness of the RAB to be about 1 μm . Such an RAB, with an ultrathin wall thickness, has excellent optical and mechanical properties. We have investigated the WGMs of the RAB microresonator by coupling WGMs through a taper fiber, as shown in Fig. 1(b). The taper fiber, with a biconical taper and a symmetrical waist, was fabricated from a conventional single-mode fiber by means of the oxyhydrogen flame direct heating method. In the experiment, the taper fiber waist, with a diameter of ~ 1 μm and near zero transmission loss character, was positioned in direct contact with the in-fiber RAB along its equator surface, as illustrated in Fig. 1(b). The light can be coupled into the RAB resonator through this taper fiber, which evanescently excites the WGMs in the RAB along its equator, and the coupling strength can be adjusted by changing the air gap between the taper fiber and the equator surface of the RAB. The WGM of the RAB resonator can be measured using the setup shown in Fig. 1(c), where the input end of the taper fiber is connected to a tunable laser source (Agilent, 81940A) via a polarization controller, and the other end is connected to an optical power meter (Agilent, N7744A).

As shown in Fig. 2, the equatorial WGMs of the RAB resonator were measured by the optical power meter with a resolution of 0.6 pm covering the wavelength range from 1550 to 1585 nm. While such equatorial WGMs have a small mode volume, they also exhibit a large azimuthal FSR between consecutive modes, and the measured azimuthal FSR is about 6.9 nm around the wavelength of 1556 nm. Here the azimuthal FSR could be expressed as [14]

$$\Delta\lambda_{\text{FSR}}^{(\text{azim})} = \lambda^2 / (2\pi n_{\text{eff}} R_0), \quad (1)$$

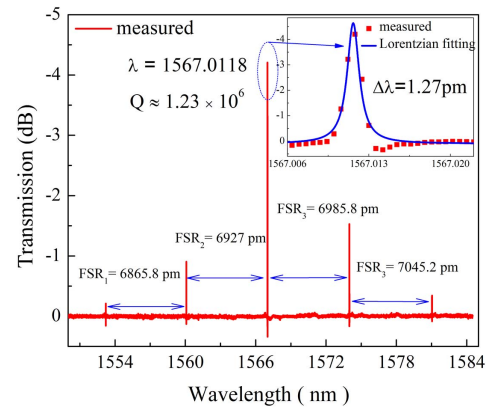


Fig. 2. Measured WGM transmission spectra with a wavelength range of 1550–1584 nm. Inset, magnified measurement data near a resonant peak (red dots) fitted with a Lorentzian curve (blue line).

where λ is the resonant wavelength, n_{eff} is the effective index of the silica, and R_0 is the radius of the RAB along the equator surface. As shown in Fig. 2, the wavelengths of the WGM resonant peaks are about 1553.219, 1560.0848, 1567.0118, 1573.9976, and 1581.0428 nm. Based on Eq. (1), the calculated R_0 is about 38.9 μm , which agrees well with the measurement result from the optical microscope image [Fig. 1(a)].

Furthermore, as shown in the inset of Fig. 2, the estimated resonance Q -factor obtained by a Lorentzian fitting is of $\sim 1.23 \times 10^6$.

In addition, it also can be seen that the transmission spectrum of the RAB resonator is near-lossless, as the measured loss is only about -0.03 dB which, owing to the factor of a very smooth inner and outer surface of the RAB ensuring better confinement of the light in a narrow ring along the equator surface by continuous total internal reflection. Note that the positive dips occurring under a 0 dB level are due to the measurement error caused by the power meter and, thus, not a real signal.

According to Eq. (1), it can be seen that any FSR interval of length $\Delta\lambda_{\text{FSR}}^{(\text{amiz})}$ contains a full set of resonances, which correspond to WGMs under different quantum numbers. For this reason, a resonator can be regarded as fully tunable if its tuning wavelength range exceeds the FSR, i.e., $\Delta\lambda_{\text{FSR}}^{(\text{amiz})}$ [14]. Thus, a resonance corresponding to any transversal WGM distribution of a fully tunable resonator can be shifted to any predetermined wavelength. To evaluate this tunable function, an experiment was set up to apply tensile strain to the RAB resonator for tuning the resonance wavelength of WGMs, as shown in Fig. 3. To apply the tensile strain to the resonator, one end of the RAB was glued on a fixed stage, and another end was fixed to a piezoelectric transducer (PZT) controlled stage. In order to measure the actual applied strain to the RAB, a broadband light source (BBS), a 3 dB fiber coupler, and an optical spectrum analyzer (OSA) with a resolution of 0.01 nm were employed to directly monitor the cavity length variation (i.e., applied tensile strains) of the RAB in real time, as shown in Fig. 3(b).

To investigate the strain-based tunability of the RAB resonator, the wavelength shift of the WGMs was measured, while the applying PZT voltage varied from 0 to 27.5 V in an increment of 2.5 V. The correlations plotted in Fig. 4(a) and its slope of the linear fitting give a tuning rate of about 31.96 pm/V with a

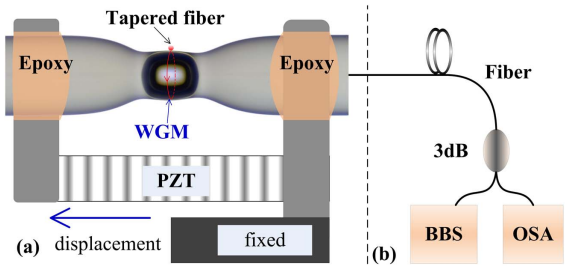


Fig. 3. (a) Illustration of the experimental setup used for applying the tensile strain to the resonator. (b) Setup used for real-time monitoring the spectral changes of a RAB FPI.

correlation factor of $R^2 \sim 0.993$ showing a good linearity of wavelength change with increasing applied voltages. The corresponding WGM resonance spectrum evolution, with increasing PZT voltage, is illustrated in Fig. 4(b), measured by the optical power meter with a resolution of 0.15 pm. As the figure shows, the coupling intensity of the WGMs has shown a fluctuation (increase or decrease), which is attributed to the position change of the probing point between the taper fiber and RAB due to the applied strain. The resonances dips shifted toward shorter wavelength, i.e., blueshift, which indicates that the equatorial radius R_0 is reduced with the PZT voltage increasing. This correlation was also proved in the numerical simulation, as shown in Fig. 6, where we clearly see that the radius R_0 is also reduced with increased tensile strain applied to the RAB. Note that here the increased PZT voltage is equivalent to the tensile strain applied to the RAB. Furthermore, the employed PZT is the model of PI-888.91 with a sub-nanometer resolution (<https://www.piceramic.com/en/>), which can respond well to milli-voltage (mV); thus, from the tuning rate of 31.96 pm/V, we can estimate that the tuning accuracy is approximately 0.03 pm.

In the experiment, due to the restriction from the extension length of the PZT, we were not able to measure the actual full tunable range of the resonator. To evaluate the full tunable range of the RAB resonator, the stretching strength of the RAB was measured as a Fabry–Perot interferometer (FPI) by manually operating the translation stage by the setup shown in Fig. 3(b). Figure 5(a) plots the FPI wavelength shift against the tensile strain, which was increased from 0 to 1000 μe with a step of 50 μe by manually stretching the RAB. From Fig. 5(a), the strain sensitivity of the RAB FPI is calculated to be 28.56 pm/ μe , corresponding to a linear fitting with a correlation factor of $R^2 = 0.99992$. Figures 5(b) and 5(c) show the

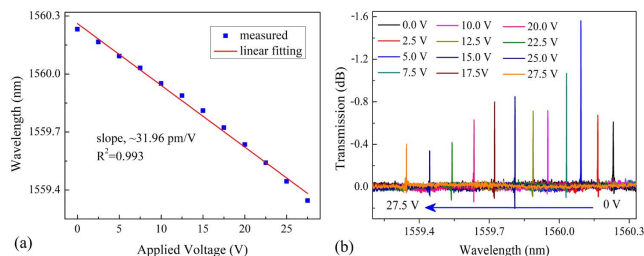


Fig. 4. (a) Applied PZT voltage to a resonator and the calculated voltage-tuning rate of about 31.96 pm/V. (b) Spectrum evolution of the resonator based on a RAB with PZT voltage increases from 0 to 27.5 V.

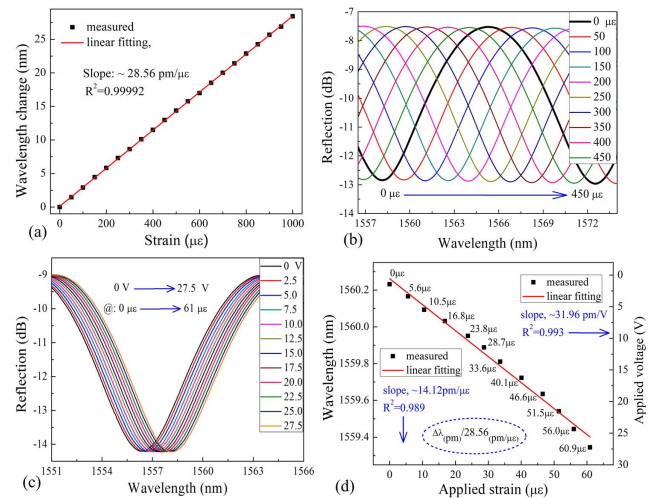


Fig. 5. (a) Strain response and (b) spectral evolution of the RAB FPI under manual stretching. (c) Spectral evolution of the RAB FPI under PZT applied voltage from 0 to 27.5 V. (d) Correlation between the voltage-tuning rate and strain-tuning rate.

spectral evolution of the RAB FPI under manual and PZT (0–27.5 V) stretching, respectively. From Figs. 5(a) and 5(c), we can build a correlation between the applied voltage and tensile strain, as plotted in Fig. 5(d). Thus, we can see that the applied PZT voltage from 0 to 27.5 V corresponds to the tensile strain from 0 to 60.9 μe . From Fig. 5(d), we can obtain a strain-tuning WGM rate to be about 14.12 pm/ μe . Although the tuning range is limited by the extension length of the PZT, according to the measured results in Fig. 5(a), the available stretch range of 1000 μe will allow a total WGM tunable range of ~ 14.12 nm for the RAB resonator, which is two times more than its azimuthal FSR of 6.9 nm. The tunability figure of merit of this RAB WGM is about $\Delta\lambda/\Delta\lambda_{\text{FSR}}^{\text{(amiz)}} \approx 2.05$.

In order to investigate the strain-based tuning mechanism of the WGM resonator, the structural deformation and stress distribution of the RAB under strain were calculated by establishing a simulation model utilizing commercial software of finite element analysis. Figure 6(a1) illustrates the three-dimensional stress distribution contour of the resonator, which is a mirror model along the equator of the RAB, with a tensile strain of 1 μe , and the colors indicate the stress distribution in different parts of the resonator. It can be seen that the maximum stress is distributed on the equator surface of the resonator, so that the equator deformation is also maximum value, which is illustrated in different views, as shown in Figs. 6(a2), 6(b2), 6(c2), and 6(c3). The vector displacement contours are shown in Figs. 6(b1) and 6(c1), and the arrows describe the directions of the resonator's deformation. At the marked points A and A' at the equator surface of the resonator in Figs. 6(a) and 6(b), it is clear that the marked points shift toward the inner center of the resonator, indicating that the equatorial radius R_0 is reduced. The calculated results also show that the resonator's equator perimeter length, used to support the fundamental mode resonance, is gradually decreasing with the tensile strain increasing. According to Eq. (1), the perimeter length is $L = 2\pi R_0$, and the changing length ΔL (red dots) is calculated by numerical simulation with the increased tensile strain, as shown in Fig. 7 (left axis). Furthermore, the measured changing

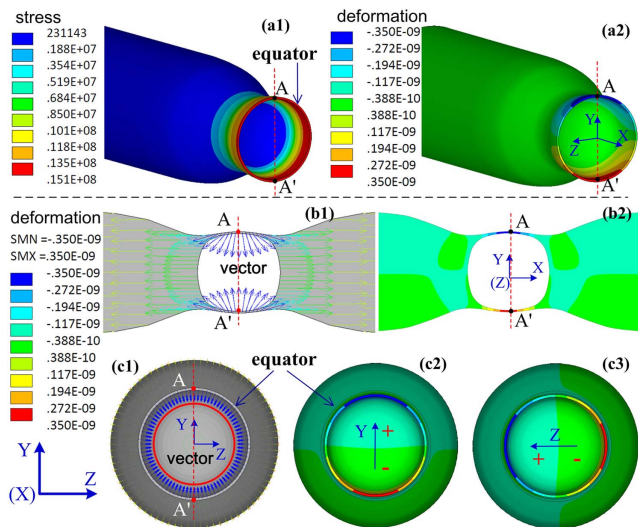


Fig. 6. (a1) Three-dimensional stress distribution contours and (a2) the stress distribution contours along the Y direction. The deformation vector field of the RAB along (b1) the transverse section and (c1) the longitudinal section. The corresponding deformation of the RAB under $1 \mu\text{e}$ strain for (b2) the transverse section (Y -axis), (c2) the longitudinal section (Y -axis), and (c3) the longitudinal section (Z -axis).

length (blue square) can be calculated by $\Delta L = \Delta\lambda(L/\lambda)$, where the strain-induced wavelength change $\Delta\lambda$ is measurable. From Fig. 7, we can clearly see that the theoretical calculation of the perimeter length change agrees very well with the measured values. Compared with other microresonators forming microbubbles, microtoroids, and microrings, the RAB resonators clearly show several advantages such as small volume, relative robustness, and high- Q ; thus, they could be more suitable for specific applications, for example, the investigation of cavity quantum electrodynamics (QED), because there is a small bubble in the resonator that may be used to contain atoms [25]. Furthermore, the RAB resonator has a simple and low-cost fabrication process, as only by using a fusion splicer to form a smaller mode volume WGM resonator.

In conclusion, we have successfully shown the implementation of a reliable continuous tuning WGM resonator based on an RAB microstructure. By changing the tensile strain applied

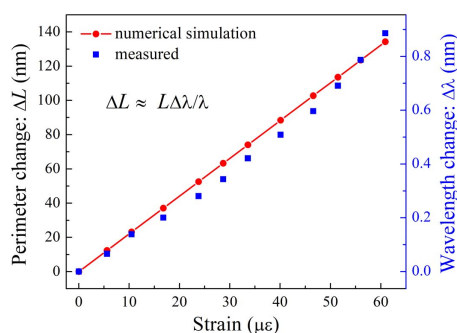


Fig. 7. Results of the numerical simulation for the perimeter change (left axis) along the equator surface of the RAB versus the applied tensile strain (red dots), reflecting a corresponding wavelength change (right axis) of the WGMs in the optical microresonator based on the RAB and comparison with the measured results (blue blocks).

to the RAB resonator, the WGM resonance can be tuned by a PZT at a rate of 31.96 pm/V (strain-tuning rate $\sim 14.12 \text{ pm}/\mu\text{e}$) with a potential tuning bandwidth of 14.12 nm , which is over two times greater than its azimuthal FSR. Furthermore, a finite element model of the resonator was created for calculating the stress and deformation distribution under varying applied tensile strain, and the calculated results have finely explained the reasons of strain tuning. This fully tunable RAB resonator has the unique advantages of a small mode volume, high quality factor exceeding 10^6 , and near-lossless WGMs.

Funding. National Natural Science Foundation of China (NSFC) (61405125, 61425007, 61635007); Natural Science Foundation of Guangdong Province (2014A030308007, 2015A030313541, 2015B010105007); Science and Technology Innovation Commission of Shenzhen (JCYJ20160427104925452, JCYJ20170412105604705, JCYJ20170818093743767); Development and Reform Commission of Shenzhen Municipality Foundation; Innovation-Leader Talent Project of Chongqing Science and Technology (CSTCCXLJR20171160).

REFERENCES

1. K. J. Vahala, *Nature* **424**, 839 (2003).
2. V. Bulovic, V. G. Kozlov, V. B. Khalfin, and S. R. Forrest, *Science* **279**, 553 (1998).
3. X. Jiang, C. Zou, L. Wang, Q. Gong, and Y. Xiao, *Laser Photon. Rev.* **10**, 40 (2016).
4. L. He, Ş. K. Özdemir, and L. Yang, *Laser Photon. Rev.* **7**, 60 (2013).
5. X. Fan, I. M. White, S. I. Shopova, H. Zhu, J. D. Suter, and Y. Sun, *Anal. Chim. Acta* **620**, 8 (2008).
6. L. He, Ş. K. Özdemir, J. Zhu, W. Kim, and L. Yang, *Nat. Nanotechnol.* **6**, 428 (2011).
7. S. Panich, K. A. Wilson, P. Nuttall, C. K. Wood, T. Albrecht, and J. B. Edell, *Anal. Chem.* **86**, 6299 (2014).
8. A. D. Boozer, A. Boca, R. Miller, T. E. Northup, and H. J. Kimble, *Phys. Rev. Lett.* **98**, 193601 (2007).
9. T. Wilk, S. C. Webster, A. Kuhn, and G. Rempe, *Science* **317**, 488 (2007).
10. F. Vollmer and S. Arnold, *Nat. Methods* **5**, 591 (2008).
11. M. S. Luchansky, A. L. Washburn, T. A. Martin, M. Iqbal, L. C. Gunn, and R. C. Bailey, *Biosens. Bioelectron.* **26**, 1283 (2010).
12. M. Sumetsky, Y. Dulashko, and R. S. Windeler, *Opt. Lett.* **35**, 898 (2010).
13. M. Pollinger, D. O'shea, F. Warken, and A. Rauschenbeutel, *Phys. Rev. Lett.* **103**, 053901 (2009).
14. M. Sumetsky, Y. Dulashko, and R. S. Windeler, *Opt. Lett.* **35**, 1866 (2010).
15. R. Madugani, Y. Yang, V. H. Le, J. M. Ward, and S. Nic Chormaic, *IEEE Photon. Technol. Lett.* **28**, 1134 (2016).
16. Z. Zhou, C. Zou, Y. Chen, Z. Shen, G. Guo, and C. Dong, *Opt. Express* **25**, 4046 (2017).
17. M. Ye, M. Shen, and X. Lin, *Opt. Express* **23**, 25846 (2015).
18. R. Henze, T. Seifert, J. Ward, and O. Benson, *Opt. Lett.* **36**, 4536 (2011).
19. M. Humar, M. Ravnik, S. Pajk, and I. Musevic, *Nat. Photonics* **3**, 595 (2009).
20. C. Yang, H. Zhang, B. Liu, S. Lin, Y. Li, and H. Liu, *Opt. Lett.* **42**, 2988 (2017).
21. M. Mur, J. A. Sofi, I. Kvasic, A. Mertelj, D. Lisjak, V. Niranjani, I. Musevic, and S. Dhara, *Opt. Express* **25**, 1073 (2017).
22. R. Chen, V. D. Ta, and H. Sun, *ACS Photon.* **1**, 11 (2014).
23. S. Liu, K. Yang, and Y. Wang, *Sci. Rep.* **5**, 7624 (2015).
24. S. Liu, Y. Wang, and C. Liao, *Opt. Lett.* **39**, 2121 (2014).
25. F. Brennecke, T. Donner, S. Ritter, T. Bourdel, M. Kohl, and T. Esslinger, *Nature* **450**, 268 (2007).